Mixed state entanglement and thermal phase transitions

Peng Liu[1,*] and Jian-Pin Wu[2,3,†]

[1]*Department of Physics and Siyuan Laboratory, Jinan University, Guangzhou 510632, China*
[2]*Center for Gravitation and Cosmology, College of Physical Science and Technology,*
Yangzhou University, Yangzhou 225009, China
[3]*School of Aeronautics and Astronautics, Shanghai Jiao Tong University, Shanghai 200240, China*

We study the relationship between mixed state entanglement and thermal phase transitions. As a typical example, we compute the holographic entanglement entropy (HEE), holographic mutual information (MI), and the holographic entanglement wedge minimum cross section (EWCS) over the superconductivity phase transition. We find that HEE, MI, and EWCS can all diagnose the superconducting phase transition. They are continuous at the critical point, but their first derivative with respect to temperature is discontinuous. MI decreases with increasing temperature and exhibits a convex behavior, while HEE increases with increasing temperature and exhibits a concave behavior. However, EWCS can exhibit either the same or the opposite behavior as MI, depending on the size of the specific configuration. These results show that EWCS captures more abundant information than HEE and MI. We also provide a new algorithm to compute the EWCS for general configurations.

I. INTRODUCTION

Quantum entanglement is the main property that distinguishes quantum systems from classical systems. Recently, quantum entanglement has become a hot topic in the fields of holographic gravity, condensed matter theory, quantum information, and so on. Many quantum entanglement measures have been found capable of diagnosing the quantum phase transition of strong correlation systems and the topological quantum phase transitions, and playing a key role in the emergence of spacetime [1–8].

There are many different types of quantum entanglement measures, such as entanglement entropy (EE), mutual information (MI), Rényi entanglement entropy, negativity, and so on. Among these quantum entanglement measures, EE has been widely accepted as a good measure for pure state entanglement. However, EE is unsuitable for measuring the entanglement of mixed states, which is way more common than pure states. Many new entanglement measures have been proposed to measure mixed state entanglement, such as the entanglement of purification (EoP), negativity, and the entanglement of formation [9,10].

---
[*]phylp@email.jnu.edu.cn
[†]Corresponding author.
jianpinwu@yzu.edu.cn

However, entanglement measures are extremely difficult to calculate.

Gauge/gravity duality provides a powerful tool for studying strongly correlated systems, and it relates entanglement related physical quantities to geometric objects in dual gravity systems. The holographic entanglement entropy (HEE) associates the EE of a subregion on the boundary with the area of the minimum surface in the dual gravity system [5]. HEE has been shown capable of diagnosing quantum phase transitions and thermodynamic phase transitions [11–21]. Recently, the Rényi entropy has been proposed to be proportional to the minimal area of cosmic branes [22]. Moreover, the butterfly effect that reflects the dynamic properties of quantum systems, has been extensively studied in holographic theory [23–32]. In addition, holographic duality of quantum complexity, a new information-related quantity from the EE, was also proposed [33–42]. More recently, the EoP was associated with the area of the minimum cross section of the entanglement wedge [43,44]. Then, the entanglement wedge minimum cross section (EWCS) has also been considered the holographic dual of some other mixed state entanglement measure, such as logarithmic negativity, reflected entropy and odd entropy [45–47]. The EWCS provides a novel and powerful tool for studying the mixed state entanglement [32,48–55].

At present, HEE has been widely studied over many different holographic phase transition models, but the research on mixed state entanglement—MI and EWCS, are still missing. For this purpose, we study the properties

of HEE, MI, and EWCS in holographic superconductivity model. We focus on the relationship between these information-related physical quantities and phase transitions and pay special attention to the difference and relationship between mixed state entanglement measures and HEE.

We organize this paper as follows: we introduce the holographic superconductivity model in Sec. II A, entanglement measures (HEE, MI, EoP) and their holographic duality in Sec. II B. We discuss the properties of HEE (III), MI (IV), and EWCS (V) systematically. In Sec. VI we discussed the critical behavior of these entanglement related quantities. Finally, we summarize in Sec. VII.

II. HOLOGRAPHIC SUPERCONDUCTIVITY PHASE TRANSITION AND HOLOGRAPHIC INFORMATION-RELATED QUANTITIES

First, we introduce the holographic model for superconductivity. Next, we introduce the HEE, MI, EoP, and their holographic dual. After that, we elaborate on the new algorithms to compute the minimum surfaces and minimum cross sections.

A. Holographic superconductivity phase transition

A thermal phase transition occurs at a finite temperature, that usually is accompanied by a symmetry breaking and the emergence of an order parameter. A prominent example of the holographic thermal phase transition is the superconductivity phase transition model. The action of the holographic superconductor is [56] (see also [57] for a recent review),

$$S = \int d^4x \sqrt{-g} \left(R + \frac{6}{L^2} - \frac{1}{2} F_{\mu\nu} F^{\mu\nu} \right.$$
$$\left. - |\nabla\Psi - iqA\Psi|^2 - m^2 |\Psi^2| \right), \qquad (1)$$

where L is the AdS length scale, A and $F = dA$ is the gauge field and the corresponding field strength. Ψ is the complex scalar field, which we write as $\Psi = e^{i\xi}\psi$ with ψ a real scalar field and ξ the Stückelberg field. We fix the gauge by setting $\xi = 0$, and the corresponding equations of motion read,

$$R_{\mu\nu} + g_{\mu\nu}(3 + \psi^2) - \left(F_{\mu\lambda} F_\nu{}^\lambda - \frac{1}{4} g_{\mu\nu} F^2 \right)$$
$$- \partial_\mu\psi\partial_\nu\psi - q^2\psi^2 A_\mu A_\nu = 0,$$
$$\nabla_\mu F^\mu{}_\nu - q^2\psi^2 A_\nu = 0, \qquad (\nabla^2 - q^2 A^2 + 2)\psi = 0. \quad (2)$$

We solve them with ansatz,

$$ds^2 = \frac{1}{z^2} \left[-(1-z)p(z)U dt^2 \right.$$
$$\left. + \frac{dz^2}{(1-z)p(z)U} + V dx^2 + V dy^2 \right],$$
$$A = \mu(1-z)a dt, \qquad (3)$$

where μ is the chemical potential of the gauge field A and $p(z) \equiv 1 + z + z^2 - \mu^2 z^3/2$. The z is the radial axis, and $z = 0, 1$ represents the AdS boundary and the horizon, respectively. The quantities U, V, a, and ψ are all functions of z, that can be obtained by solving the equations of motion (2). The system has a simple solution with $a = U = V = 1, \psi = 0$, where the system goes back to the AdS-RN black brane. The ψ has the following expansion near the AdS boundary,

$$\psi = \psi_1 z + \psi_2 z^2 + \cdots, \qquad (4)$$

where ψ_1 is the source of the condensate, that we set as 0 such that ψ emerges as spontaneous condensate. ψ_2 stands for the expectation value of an operator O_2 dual to ψ,

$$\langle O_2 \rangle = \sqrt{2}\psi_2, \qquad (5)$$

that represents the condensate.

The Hawking temperature is $\tilde{T} = \frac{6-\mu^2}{8\pi}$. The system is invariant under the following rescaling,

$$(t, x, y) \to \alpha^{-1}(t, x, y), \qquad V \to \alpha^2 V,$$
$$\mu \to \alpha\mu, \qquad \tilde{T} \to \alpha\tilde{T}. \qquad (6)$$

In this paper, we adopt μ as the scaling unit,[1] and the dimensionless Hawking temperature $T = \tilde{T}/\mu$. At first glance, the expression of $\tilde{T}$ may be contrary to the scaling relation in (6), but this expression is correct. The reason is that the more familiar coordinate system is (t, r, x, y), in which the background solution should be related to the radius r_h of the black brane horizon. Because the system has rescaling symmetry, we fix $r_h = 1$ in $z \equiv r_h/r$ coordinate to facilitate calculation. This method has been adopted in [16–18], and the results are consistent with the results of earlier literature [58]. For concreteness, we fix $L = 1, m^2 = -2$ and $q = 10$ where the critical temperature $T_c = 0.150296$. We show the condensate $\sqrt{\langle O_2 \rangle}/\mu$ vs T in Fig. 1. There is a scaling relationship $\sqrt{\langle O_2 \rangle}/\mu \sim t^{\alpha_{\text{cond}}}$, between the condensate near the critical point and the reduced temperature

$$t \equiv 1 - \frac{T}{T_c}, \qquad (7)$$

---

[1]This is equivalent to choosing the grand canonical ensemble to describe the system.
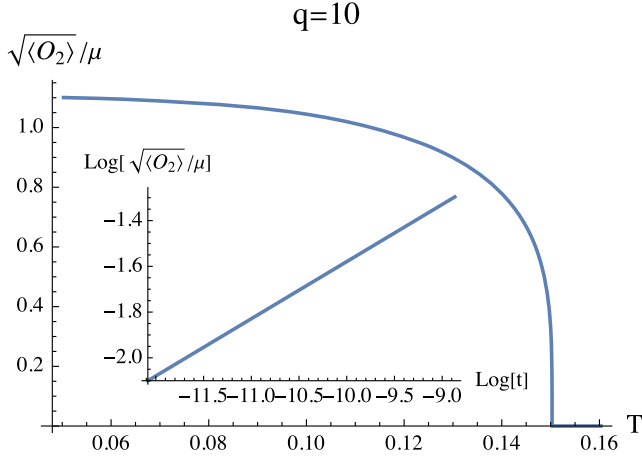
FIG. 1. The condensate at $q = 10$. The critical temperature $T_c = 0.150296$, below which the system is in the superconducting phase. The inset plot is the logarithm of the condensate vs the logarithm of the reduced temperature t.

and the critical exponent is $\alpha_{\mathrm{cond}} = 1/4$ [59]. In fact, the critical exponent is completely determined by the fundamental symmetry of the model. As shown in the illustration in Fig. 1, there is an obvious linear relationship between the logarithm of the condensate and the reduced temperature near the critical temperature. Moreover, our numerical results show that the slope is about 0.2499, which is consistent with the results of holographic superconductivity.

B. Holographic information-related quantities

One of the most striking features of quantum mechanics is entanglement. The most famous measure of entanglement is EE, which measures the entanglement between a subsystem and its complement. Specifically, the EE S_A between A and B in $A \cup B$ is defined as von Newmann entropy in terms of the reduced density matrix ρ_A,

$$S_A(|\psi\rangle) = -\mathrm{Tr}[\rho_A \log \rho_A], \qquad \rho_A = \mathrm{Tr}_B(|\psi\rangle\langle\psi|). \quad (8)$$

For pure states we will find that $S_A = S_B$ [60]. In holographic duality theory, the HEE was related to the area of the minimum surface in dual gravity systems [5] (see the left plot of Fig. 3). HEE usually diverges due to the existence of asymptotic AdS boundary. The commonly used regulation is to subtract the common UV divergent term brought by the asymptotic AdS from HEE to get the UV finite term. In this paper, we also adopt this scheme and all HEE labeled by S will be the finite term of HEE.

EE has been widely accepted as a good measure of pure state entanglement. However, EE is not a good measure of mixed state entanglement. For instance, A and B in a system formed by the direct product of density matrix ρ_A and ρ_B does not entangle with each other but can have nonzero EE. The reason is that EE not only takes into

account the quantum entanglement but also the classical correlation. Many new measures of the mixed state entanglement have been proposed [9,10], among which the most direct measure of mixed state entanglement is the mutual information (MI).

For separate $A \cup C$ separated by B, the MI is defined as
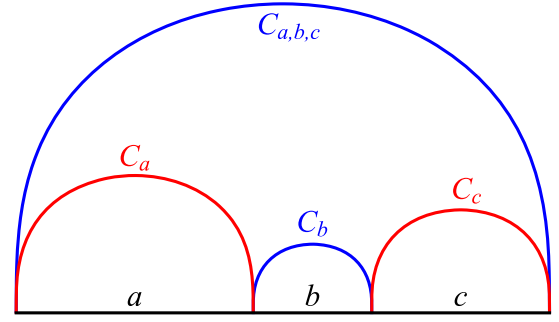
FIG. 2. The illustration of the mutual information.

$$I(A, C) := S(A) + C(B) - \min(S(A \cup C)), \quad (9)$$

which measures the entanglement between A and C. It is easy to verify that $I(A, C) = 0$ when $\rho_{AC} = \rho_A \otimes \rho_C$. Therefore, MI exhibits the important property that the direct product state has zero entanglement. However, MI is also not a perfect measure for mixed state entanglement. Since MI is defined by EE in essence, [48] points out that the properties of MI in some cases are completely dominated by EE or even thermal entropy. This shows that we need to resort to other mixed state entanglement measures. Since $S(A \cup C)$ can have two different configurations, the connected case (blue curves) and the disconnected case (red curves) are shown in Fig. 2. The (a, b, c) and $C_\#$ are the width of the A, B, C and the minimum surface associated with them, respectively. Apparently, when the area of the disconnected case is smaller than the area of the connected case, the MI vanishes. The critical point across which the MI starts to vanishes is called the disentangling phase transition.

The EoP, which involves the purification of mixed states, is a new mixed state entanglement measure that is currently being extensively studied. The density matrix ρ of a mixed state on $\mathcal{H}_A \otimes \mathcal{H}_B$ can be purified by introducing two extra systems A' (entangled with A) and B' (entangled with B) such that ρ emerges as the reduced matrix from a pure state $|\psi\rangle \in \mathcal{H}_{AA'} \otimes \mathcal{H}_{BB'}$. There are infinite ways to purify the ρ, and the EoP $E_p(\rho)$ is defined as the minimum EE between AA' and BB' [61]

$$E_p(\rho) := \min_{|\psi\rangle : \rho = \mathrm{Tr}_{A'B'} |\psi\rangle\langle\psi|} S_{AA'}(|\psi\rangle). \quad (10)$$

EoP has been shown to satisfy several important inequalities [61]. Therefore, a reliable holographic dual must also satisfy these inequalities [43,62]. Takayanagi *et al.*
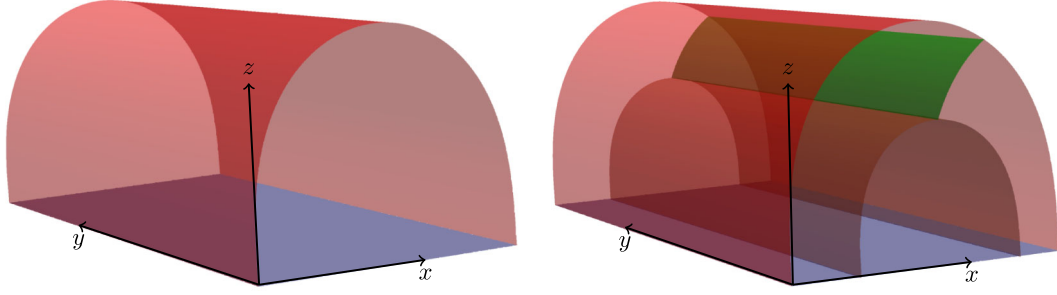
FIG. 3.   The left plot: The minimum surface for a given width w. The right plot: The minimum cross section (green surface) of the entanglement wedge.

proposed a holographic dual of the EoP $E_W(\rho_{AB})$ as the area of the minimum cross section Σ_{AB} in connected entanglement wedge [43], i.e., the configurations with nonzero MI (see the right plot in Fig. 3),

$$E_W(\rho_{AB}) = \min_{\Sigma_{AB}}\left(\frac{\mathrm{Area}(\Sigma_{AB})}{4G_N}\right). \quad (11)$$

For a biparty system $A \cup C$ separated by B (see Fig. 2), the entanglement wedge is defined as the region surrounded by the minimum surfaces and $A \cup C$. It is worth noting that the EoP, i.e., the minimum cross section can only exist in the connected entanglement wedge. For disconnected cases where MI vanishes, the EoP also vanishes. Recently, EWCS has also been considered as a holographic dual of logarithmic negativity, reflected entropy and odd entropy [45–47].

The EWCS lives in the entanglement wedge that relates to the minimum surfaces. Therefore, we provide new algorithms to obtain the minimum surfaces and the EWCS.

C. Computations of holographic EWCS

For the convenience of numerics, we study the EWCS of infinite strips in homogeneous background. For a generic homogeneous background

$$ds^2 = g_{tt}dt^2 + g_{zz}dz^2 + g_{xx}dx^2 + g_{yy}dy^2, \quad (12)$$

with $z = 0$ denoting the asymptotic AdS boundary, the left plot in Fig. 3 is the cartoon of the minimum surface for an infinite strip along y-axis. The homogeneity requires that all metric components $g_{\mu\nu}$ are functions of z only. HEE, MI, and EWCS all have the same scaling dimension, and we divide them by μ to obtain the dimensionless quantities. The scaling dimension comes from the area obtained by integrating over y-direction $\int dy = L_y$, which we omit for convenience. Therefore, HEE, MI, and EWCS all have the same scaling dimension as that of μ.

In previous work [51], we used NDSolve with *Mathematica* to develop an algorithm to solve the minimum surface and the corresponding asymmetric EWCS.

We adopted the arc-length parameter and took full advantage of homogeneity to accelerate the solution of EWCS, and applied this algorithm to calculate asymmetric EWCS in AdS$_4$ space-time and AdS-RN black hole systems. However, we encountered some limitations with this algorithm. First of all, choosing the arc-length parameter will make it difficult to solve the minimum surface in the asymptotic AdS region. Second, NDSolve method fails easily in the near horizon region due to the coordinate singularity. As a result, this algorithm can only offer reliable numerical EWCS results in a relatively narrow range of parameters. In this paper, we propose new algorithms to calculate the minimum surface and asymmetric EWCS, that will render the numerical computation much more stable and reliable.

1. The minimum surface

The minimum surface near the AdS boundary is perpendicular to the boundary, which renders the spatial direction x an unsuitable parameter for solving the minimum surface. References [54,63] adopted the angle θ with $\tan\theta = z/x$, as the parameter of the minimum surface (see Fig. 4). As shown in Fig. 4, the homogeneity of the background ensures that the minimum curve is symmetrical about the middle vertical line, which renders θ, the angle between the line from the origin to the point on the curve and the x-axis, a good parametrization of the curve. The angle θ ranges between $[0, \pi/2]$, and the full solution on $[0, \pi]$ can be obtained by mirroring the solution on $[0, \pi/2]$ to $[\pi/2, \pi]$. We follow this method, and a surface can be parametrized as $(x(\theta), z(\theta))$ with area A given by

$$A = 2\int_0^{\pi/2}\sqrt{x'(\theta)^2 g_{xx}g_{yy} + z'(\theta)^2 g_{yy}g_{zz}}\,d\theta. \quad (13)$$

The resultant equations of motion read,

$$x'(\theta)z'(\theta)^2\left(\frac{g'_{xx}}{2g_{xx}} + \frac{g'_{yy}}{g_{yy}} - \frac{g'_{zz}}{2g_{zz}}\right) + \frac{x'(\theta)^3(g_{yy}g'_{xx} + g_{xx}g'_{yy})}{2g_{xx}g_{zz}}$$

$$+ x''(\theta)z'(\theta) - x'(\theta)z''(\theta) = 0, \quad z(\theta) - \tan(\theta)x(\theta) = 0,$$

$$(14)$$
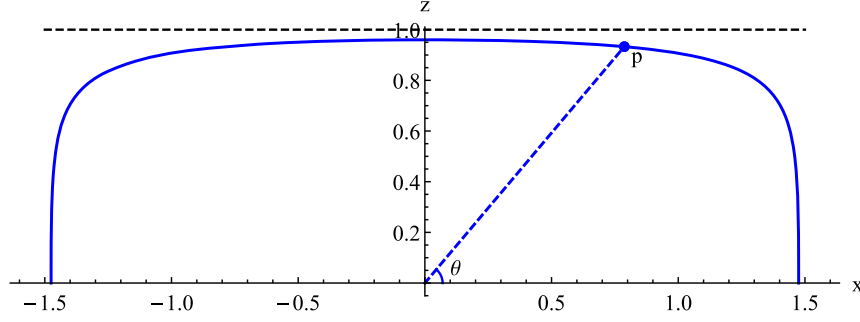
FIG. 4. The angle as the parameter of the minimum surface. The horizontal black line is the horizon ($z = 1$).

where $g'_{\#\#} \equiv g'_{\#\#}(z)$. However, it seems that the second equation in (14) can be substituted into the first equation to eliminate $x(\theta)$ or $z(\theta)$. This is feasible in principle. However, the singularity of $\tan(\pi/2)$ and possible $\tan(0)$ in the denominator will plague the numerics. Therefore, we adopt the seemingly redundant formalism in order to obtain a precise enough solution. The boundary conditions are

$$z(0) = 0, \quad x(0) = w, \quad z'(\pi/2) = 0, \quad x(\pi/2) = 0, \quad (15)$$

where w is the width of the infinite strip. Also, $x(\pi/2) = 0$ constraint the origin $x = 0$ as the middle of the minimum surface, and $z'(\pi/2) = 0$ reflects the fact that the minimum surface symmetry about the middle of the minimum surface.

In order to solve (14) with first order boundary condition (15), we discretize the θ with finite difference method[2] and attack the nonlinearity with the Newton-Raphson iteration method. These methods are also used in [16–18] to solve numerical holographic systems. Compared with the built-in NDSolve, this method is insensitive to the coordinate singularity of the near-horizon geometry, thus improving the accuracy of the minimum surface solution. Based on the minimum surfaces, we use the Newton-Raphson iteration method again to solve the area of the minimum cross section between the two minimum surfaces, i.e., the EoP.

2. The EWCS

In [51], we transform the solution of EWCS into a problem of solving the minimum value in two-dimensional space. In fact, the globally minimum cross section must be orthogonal to the minimum surface at the intersections, since a global minimum must also be a local minimum. This local constraint can be used to accelerate the search of the minimum cross section since it does not need to compute the arc length.

---

[2]One should choose the Gauss-Lobatto allocation for better numerical convergence. The full-order finite difference method on the Gauss-Lobatto allocation is essentially equivalent to the pseudo-spectral method using Chebyshev basis [64]. For problems with moving endpoints, the finite difference method is more flexible.

Given a biparty subsystem with minimum surfaces $C_1(\theta_1), C_2(\theta_2)$, we solve the minimum surface C_{p_1,p_2} connecting $p_1 \in C_1$ and $p_2 \in C_2$. We parametrize C_{p_1,p_2} with z, then the area of C_{p_1,p_2} reads,

$$A = \int_{C_{p_1,p_2}} \sqrt{g_{xx}g_{yy}x'(z)^2 + g_{zz}g_{yy}}\,dz. \quad (16)$$

The resultant equation of motion becomes,

$$x'(z)^3 \left(\frac{g_{xx}g'_{yy}}{2g_{yy}g_{zz}} + \frac{g'_{xx}}{2g_{zz}} \right)$$
$$+ x'(z)\left(\frac{g'_{xx}}{g_{xx}} + \frac{g'_{yy}}{2g_{yy}} - \frac{g'_{zz}}{2g_{zz}} \right) + x''(z) = 0, \quad (17)$$

with boundary condition,

$$x(z(\theta_1)) = x(\theta_1), \qquad x(z(\theta_2)) = x(\theta_2). \quad (18)$$

We show in Fig. 5 the methods for solving the EWCS. The perpendicular conditions at the endpoints read,

$$g_{ab}\left(\frac{\partial}{\partial z}\right)^a \left(\frac{\partial}{\partial \theta_1}\right)^b \bigg|_{p_1} = 0, \qquad g_{ab}\left(\frac{\partial}{\partial z}\right)^a \left(\frac{\partial}{\partial \theta_2}\right)^b \bigg|_{p_2} = 0. \quad (19)$$

Now, solving the EWCS is to find the minimum surface ending at (θ_1, θ_2) where (19) is satisfied. Notice that vectors $\frac{\partial}{\partial z}, \frac{\partial}{\partial \theta_1}, \frac{\partial}{\partial \theta_2}$ are not normalized, for numerical stability it is better to implement the perpendicular conditions with normalized vectors as,

$$Q_1(\theta_1, \theta_2) \equiv \frac{g_{ab}\left(\frac{\partial}{\partial z}\right)^a \left(\frac{\partial}{\partial \theta_1}\right)^b}{\sqrt{g_{cd}\left(\frac{\partial}{\partial z}\right)^c \left(\frac{\partial}{\partial z}\right)^d}\sqrt{g_{mn}\left(\frac{\partial}{\partial \theta_1}\right)^m \left(\frac{\partial}{\partial \theta_1}\right)^n}}\bigg|_{p_1} = 0,$$

$$Q_2(\theta_1, \theta_2) \equiv \frac{g_{ab}\left(\frac{\partial}{\partial z}\right)^a \left(\frac{\partial}{\partial \theta_2}\right)^b}{\sqrt{g_{cd}\left(\frac{\partial}{\partial z}\right)^c \left(\frac{\partial}{\partial z}\right)^d}\sqrt{g_{mn}\left(\frac{\partial}{\partial \theta_2}\right)^m \left(\frac{\partial}{\partial \theta_2}\right)^n}}\bigg|_{p_2} = 0.$$

$$(20)$$
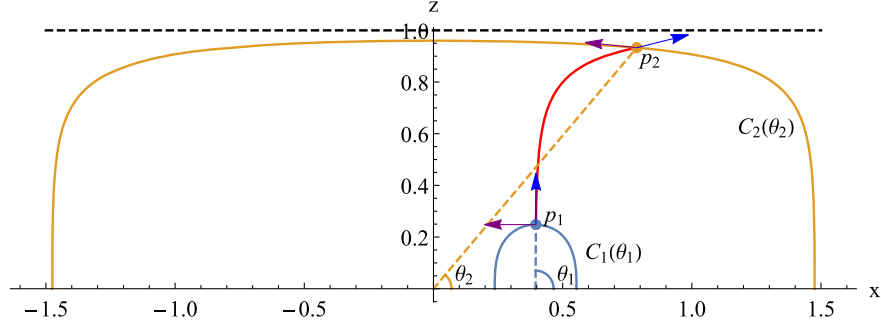
FIG. 5. The demonstration of the EWCS. The p_1 and p_2 are the intersection points of the minimum surface connecting those two minimum surfaces. The solid blue curve (parametrized with θ_1) and solid orange curve (parametrized with θ_2) are minimum surfaces. The thick red curve is the minimum surface connecting p_1 and p_2. The blue arrows at the p_1 and p_2 are the tangent vector $(\frac{\partial}{\partial z})^a|_{p_1}$ and $(\frac{\partial}{\partial z})^a|_{p_2}$ along the C_{p_1,p_2}, while the purple arrows are the tangent vectors $(\frac{\partial}{\partial \theta_1})^a|_{p_1}$ and $(\frac{\partial}{\partial \theta_2})^a|_{p_2}$ along C_1, C_2, respectively. The dark dashed horizontal line is the horizon.

Note that Q_1 and Q_2 are both functions of the θ_1 and θ_2. Now, the search of the EWCS is equivalent to finding the minimum surface ending at (θ_1, θ_2) where (20) is satisfied.

To find the EWCS, we implement the Newton-Raphson method, that we describe below.

(1) Prepare initial values of the angles $(\theta_1^{(0)}, \theta_1^{(0)})$, and solve the minimum surface connecting p_1 and p_2, and compute the Q_1 and Q_2.

(2) To find the (θ_1, θ_2) such that $Q_1 = Q_2 = 0$, we deduce the correction $\delta\theta_1, \delta\theta_2$ using the Newton-Raphson method as,

$$\begin{pmatrix} Q_1 \\ Q_2 \end{pmatrix} + \begin{pmatrix} \partial_{\theta_1} Q_1 & \partial_{\theta_2} Q_1 \\ \partial_{\theta_1} Q_2 & \partial_{\theta_2} Q_2 \end{pmatrix} \begin{pmatrix} \delta\theta_1 \\ \delta\theta_2 \end{pmatrix} = 0. \qquad (21)$$

The Jacobian element can be approximated with $\partial_{\theta_i} Q_j \simeq \frac{Q_j(\theta_i + \delta\theta_i) - Q_j(\theta_i)}{\delta\theta_i}$, which requires solving the minimum surface at least three times.

(3) Solve the linear equation (21), and obtain the corrections $(\delta\theta_1, \delta\theta_2)$. Update θ_1, θ_2 with $(\theta_1, \theta_2) = (\theta_1, \theta_2) + (\delta\theta_1, \delta\theta_2)$.

(4) Iterate the above three steps, until $Q_1 = 0$ and $Q_2 = 0$ is satisfied within the error bound. In this paper, we set the error bound as 10^{-6}, where only solutions with $|Q_i| < 10^{-6}$ are accepted.

A careful choice of the initial values (θ_1, θ_2) is needed for the iterations to converge. The numerical reliability is guaranteed by the convergence of the results when setting different initial values or increasing the density of discretization (see [64] for more technical details). Compared with the previous method, the current method is more advanced in the following aspects,

(1) The iteration is fast as long as we iterate a solution with a good initial value. A good strategy is to use a solution as the initial solution when solving a problem with parameters nearby.

(2) The solution is more precise compared with the previous method. In this paper, we can obtain results with $|Q_i| \sim 10^{-7}$.

(3) It does not suffer from the coordinate singularity like the previous method, and hence the results are much more stable. This means that it can obtain solutions in a larger range of parameters.

In principle, there may be multiple local minimums when searching for the minimum cross section, thus different initial values need to be assigned to test this point. In this paper, we obtained the same results for many different initial values, which shows that the area of the cross section should be globally convex in the parameter space (θ_1, θ_2). Next, the endpoint on the inner curve (see the blue curve $C_1(\theta_1)$ in Fig. 5) should end on the regions near the top. Otherwise, the area of the minimum cross section will be very large due to the dilation from the AdS boundary. This ruled out the possibility for densely distributed local minimums. It is also not possible for sparsely distributed local minimums, because the endpoint on the inner curve is unique, and the local perpendicular condition will dictate the minimum cross section. In addition, a different algorithm that searches the whole parameter space of the cross sections shows that the area of the cross section is indeed a globally convex function for AdS-RN black branes, Gubser-Rocha model and Lifshitz black branes [49–51]. However, for double holography [65–67] or AdS/BCFT [68] where multiple boundaries may exist, the minimum cross section may end on multiple alternative minimum surfaces instead of the outer curve $C_2(\theta_2)$ in Fig. 5. Our algorithms can be generalized to compute the correct EWCS by dealing with the various candidates separately, and choosing the global minimum from them.

Next, based on the above techniques, we explore the relationship between HEE, MI, EWCS and phase transition, as well as the comparison between them.
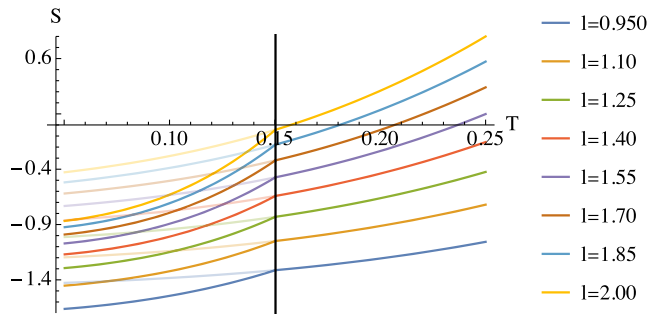
FIG. 6. The HEE vs T at different values of l specified by the plot legends. The black vertical line labels the critical temperature. Below the critical temperature, the segments with deeper and lighter colors correspond to the HEE of the solutions with superconductivity condensate, and the AdS-RN background, respectively.

III. THE HOLOGRAPHIC ENTANGLEMENT ENTROPY

Figure 6 shows the relationship between HEE and temperature in the critical region. As can be seen from Fig. 6, HEE is continuous at the critical point, but its first derivative with respect to T is discontinuous. In addition, HEE increases with increasing temperature in the critical region. These phenomena do not depend on the width l of the infinite strip. It has been shown that the larger the width of the infinite band, the greater the contribution of thermodynamic entropy in HEE [29]. Therefore the thermodynamic entropy, as a quantity which only depends on the near horizon geometry, should also diagnose the superconducting phase transition. This is certified in Fig. 7, where the thermal entropy density s indeed show similar phenomena as the HEE.

The above phenomena show that both HEE and the thermal entropy are good diagnoses of the thermal phase transition. This is as expected since the thermal phase transition is always accompanied by the emergence of condensate. Such condensate will introduce new degrees of
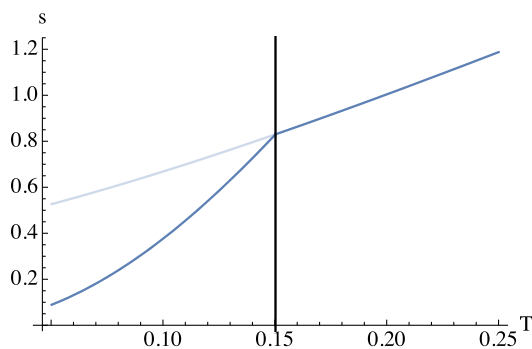
freedom to the system, and hence radically change the thermal entropy properties, as well as the EE. Similar phenomena of the HEE over superconductivity phase transition have been obtained in [69–72].

With the HEE, the MI is readily computed.

IV. THE HOLOGRAPHIC MUTUAL INFORMATION

The MI, originated from the EE, should also reflect the thermal phase transition. Figure 8 shows the relationship between MI and temperature in the critical region. First, MI decreases with increasing temperature, which is opposite to the relationship between HEE and temperature. Second, similar to HEE, MI can diagnose phase transitions indeed. MI is continuous at the critical point, but its first derivative with temperature is discontinuous. In addition, when the temperature increases, the MI may decrease to zero, which is called the disentangling phase transition. This can be understood as that thermal effects may destroy the quantum entanglement. Also, the system disentangles more easily for smaller values of c when fixing the a, b.

An interesting quantity related to the disentangling phase transition is the critical size of the configurations. We demonstrate the critical c (labeled as c_c) in Fig. 9, in which we see that the critical c increases with the increasing
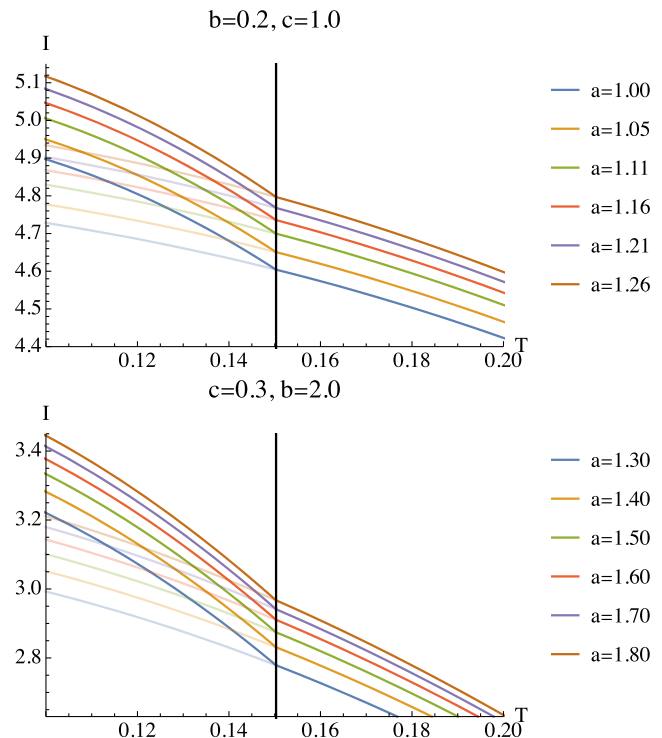
FIG. 8. The MI vs T. The black vertical line labels the critical temperature. Below the critical temperature, the segment with deeper and lighter color correspond to the MI of the solutions with superconductivity condensate, and the AdS-RN background, respectively.

FIG. 7. The entropy density s vs T. The black vertical line labels the critical temperature. Below the critical temperature, the segment with deeper and lighter color correspond to the entropy density of the solutions with superconductivity condensate, and the AdS-RN background, respectively.
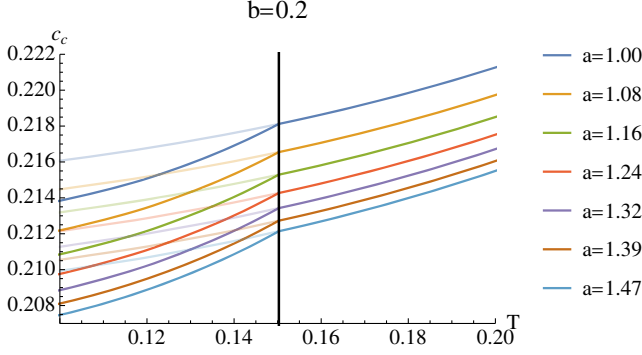
FIG. 9. The critical c, where the vertical line represents the critical temperature. Below the critical temperature, the segment with deeper and lighter color correspond to the critical c of the solutions with superconductivity condensate, and the AdS-RN background, respectively.

temperature. This is in accordance with the phenomena observed in Fig. 8.

Another notable feature is that MI is always convex in the critical region. In contrast, HEE is concave. The opposite behavior of MI and HEE is essentially due to their association on definition. EWCS is different from MI and HEE by definition, thus its behavior in the critical region is worth exploring.

V. THE ENTANGLEMENT WEDGE MINIMUM CROSS SECTION

In this section, we first explore the EWCS behavior in the critical region to reveal the relationship between EWCS and phase transition. Subsequently, we will verify that the EWCS in this paper still satisfies some important inequalities.

A. EWCS and thermal phase transition

Similar to HEE and MI, EWCS also shows obvious unsmoothness at the critical point. As shown in Fig. 10, EWCS is continuous, but its first derivative is discontinuous at the critical point. Moreover, EWCS decreases with increasing temperature, which is consistent with MI. In addition, it can exhibit convex behavior in the critical region like MI. Intriguingly, EWCS can also exhibit concave behavior (as shown in Fig. 11). This is a key difference between EWCS and MI.

Whether the EWCS is convex or concave depends on specific configurations. By comparing the Fig. 10 and Fig. 11 where the configurations of (a, b, c) have been chosen as the same as that of MI in Fig. 8, we can find that when the configuration is relatively small and the minimum cross section is far away from the horizon, the EWCS exhibits a convex behavior similar to that of MI. However, when the configuration is relatively large, where the minimum cross section is close to the event horizon of the black hole, the EWCS will show a concave behavior.

The difference between EWCS and MI shows that EWCS, as a measure of mixed state entanglement, characterizes different information of a quantum system. Moreover, the configuration-dependent properties of EWCS show that EWCS exhibits more abundant phenomena than MI, which may reveal the properties of quantum entanglement more comprehensively.

Another interesting phenomenon is the angle (endpoint) behavior in the critical region. From Fig. 12 we find that the angle parameter can work as a good diagnose of the phase transition by showing a rapid turn in the space of the (θ_1, θ_2). Also, the typical change of θ when variating the T is of order 10^{-4}, which has been well captured by our numerics that is precise up to 10^{-7}. When changing T, the θ_{m1} changes very slowly, while the θ_{m2} changes relatively more rapidly. This is as expected, since the point p_1 parametrized by θ_{m1} locates at the regions near the boundary, where the major contribution to EWCS lies. Therefore, it will change less than that of the p_2 (parametrized by θ_{m2}) region, which is relatively far away from the boundary.
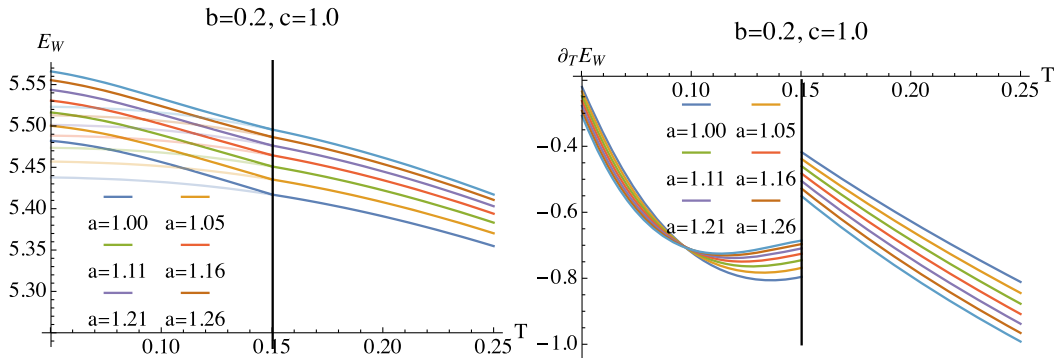
FIG. 10. The EWCS E_W and the first-order temperature derivative with respect to E_W vs the temperature. These two plots are obtained at $(b, c) = (0.2, 1)$ at different values of c specified by the plot legends. Here, the E_W is convex. In the left plot, below the critical temperature, the segment with deeper and lighter color correspond to the E_W of the solutions with superconductivity condensate, and the AdS-RN background, respectively.
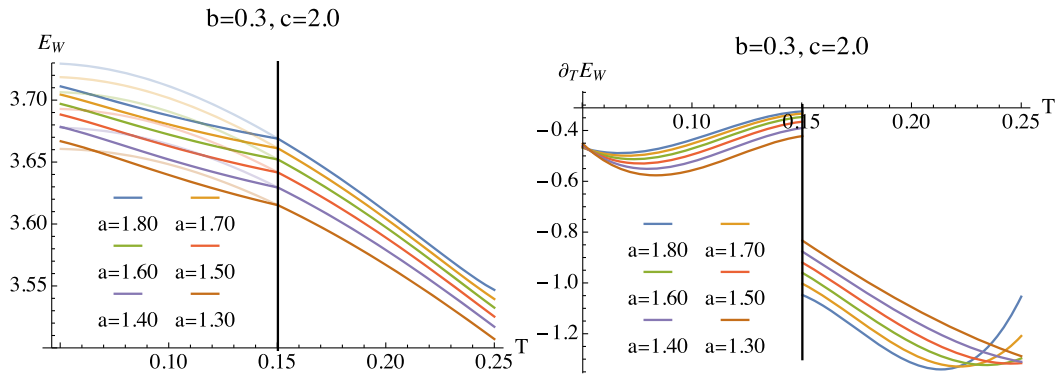
FIG. 11.   The EWCS E_W and the first-order temperature derivative with respect to E_W vs the temperature. These two plots are obtained at $(b, c) = (0.3, 2)$ at different values of c specified by the plot legends. Here, the E_W is concave. In the left plot, below the critical temperature, the segment with deeper and lighter color correspond to the E_W of the solutions with superconductivity condensate, and the AdS-RN background, respectively.

B. Inequalities of EWCS

The EWCS satisfies several important inequalities, that the correct holographic EWCS expression must satisfy.
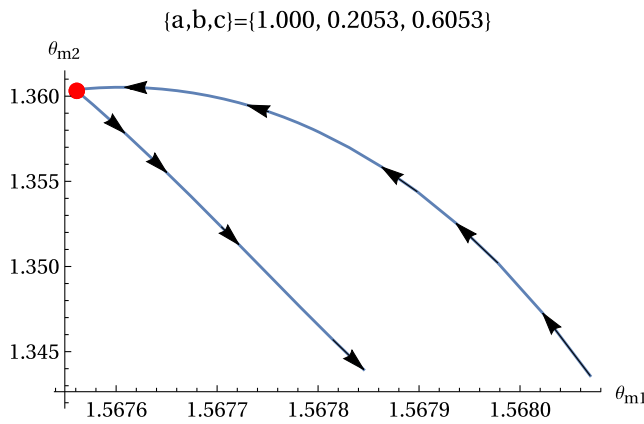
FIG. 12.   The endpoints of the corresponding EWCS for different values of temperature. Along the arrow direction, the temperature increases, and the turning point (red point) exactly matches the critical temperature.
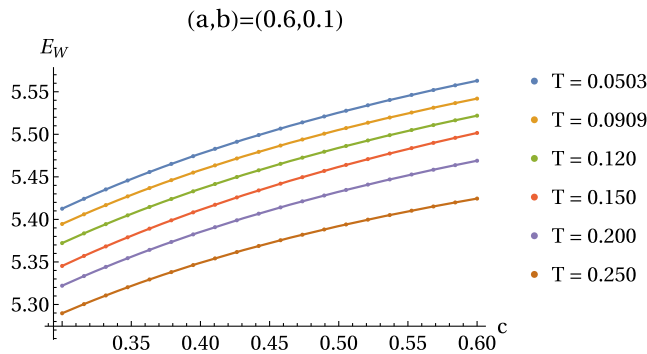
FIG. 13.   EWCS vs c. Apparently, the EWCS decreases with the temperature. Also, EWCS increases as the c increases, this is one of the inequalities that EWCS has to satisfy.

The first inequality is

$$E_W(\rho_{A(BC)}) \geq E_W(\rho_{AB}) \qquad (22)$$

which has been shown with the entanglement wedge nesting property [43]. The inequality (22) can be translated into

$$E_W(a, b, c + \delta c) \geq E_W(a, b, c) \quad \text{with} \quad \delta c \geq 0. \qquad (23)$$

This is readily seen in Fig. 13, where we can find that E_W indeed increases with increasing c at fixed values of a, b and T.

The second inequality is,

$$E_W(\rho_{AC}) \geq \frac{1}{2} I(A, C), \qquad (24)$$

which states that E_W of any configuration is greater than half of the MI. This is shown in Fig. 14, where the data of
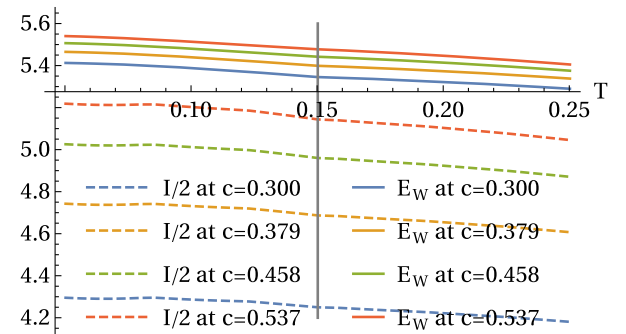
FIG. 14.   EWCS vs $I/2$. The solid lines and the dashed lines are the EWCS and one-half of the MI at different values of c, respectively. At a fixed value of c, the solid line and the dashed line are of the same color. It is readily seen that EWCS is always greater than one-half of the MI. In this plot we fix $(a, b) = (0.6, 0.1)$.
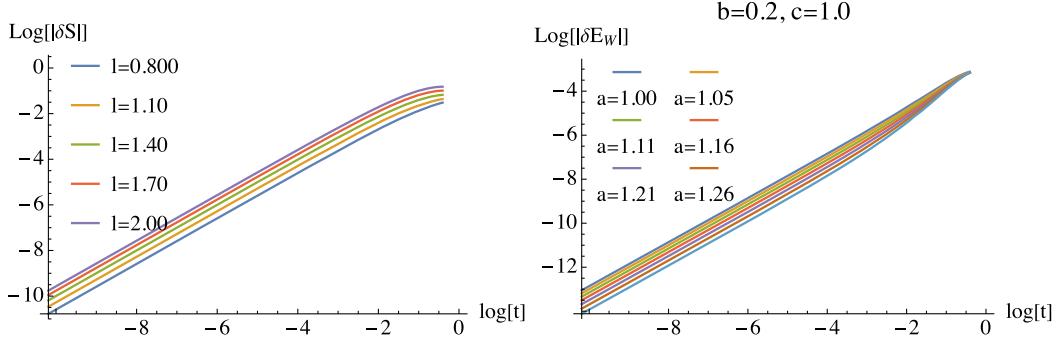
FIG. 15. The left and right plot are $\ln(t)$ vs $\ln(|\delta S|)$ and $\ln(t)$ vs $\ln(|\delta E_W|)$, respectively.

the solid curves (EWCS) of a certain color is always larger than that of the dotted curves (EWCS) of the same color.

The above two phenomena show that the EWCS in this paper does satisfy the important inequalities. These results once again enhance the reliability of holographic EWCS prescription.

VI. THERMAL PHASE TRANSITIONS AND GEOMETRICAL OBJECTS

In the above three sections, we discussed in detail the relationship between the three entanglement-related quantities HEE, MI and EWCS and the superconductivity phase transition. On the one hand, they exhibit very similar discontinuities on the temperature derivatives. On the other hand, EWCS has more abundant behaviors than HEE and MI. Next, we discuss in detail the relationship between these behaviors and superconducting phase transition.

The critical scaling behavior is a typical characteristic of most phase transitions. For example, the condensate of superconducting phase transitions has a critical exponent of $1/4$. Therefore, it is worth discussing whether HEE, MI and EWCS also have scaling behavior. Our numerical results show that they not only have perfect scaling behavior but also have exactly the same critical exponents. The critical temperature is the bifurcation point of the system, under which the system has both AdS-RN solution and superconducting condensate solution. After the phase transition, its HEE, MI and EWCS will change obviously. We subtract them from the counterpart of the AdS-RN branch and study the critical behavior of this difference (i.e., the difference between the deeper and lighter curves in previous figures) near the critical point, as we stated in Eq. (25).

$$\delta S = S_{\text{cond}} - S_{\text{AdS-RN}}, \qquad \delta I = I_{\text{cond}} - I_{\text{AdS-RN}},$$
$$\delta E_W = E_{W\text{cond}} - E_{W\text{AdS-RN}}. \qquad (25)$$

We label the critical behavior as,

$$\delta S \sim t^{\alpha_{\text{HEE}}}, \qquad \delta I \sim t^{\alpha_{\text{MI}}}, \qquad \delta S \sim t^{\alpha_{\text{EWCS}}}. \quad (26)$$

Consequently, the $\ln(|\delta S|), \ln(|\delta I|), \ln(|\delta E_W|)$ will have linear dependence on $\ln(t)$ with the critical exponent being the slope. Due to the definition of MI (9), we can directly deduce that $\alpha_{\text{HEE}} = \alpha_{\text{MI}}$. Therefore, we only need to study α_{HEE} and α_{EWCS}.

We show the results in Fig. 15, from which we can see that HEE and EWCS have obvious scaling behavior near the critical point. Moreover, the numerical results show that the critical exponents of HEE and EWCS are extremely close to 1. That is to say, we will have

$$\alpha_{\text{HEE}} = \alpha_{\text{MI}} = \alpha_{\text{EWCS}} = 1. \qquad (27)$$

These phenomena indicate that HEE, MI and EWCS all have the same scaling behavior in the holographic superconducting phase transition. Next, we will prove this result analytically. In fact, we will show that not only HEE, MI and EWCS, any physical quantity that only depends on the geometry will have the same critical exponent 1.

At the onset of the phase transition, only the perturbation of the complex scalar field needs to be turned on. This method can be used to analyze the critical point of superconducting phase transition. The background perturbation will only appear in the second-order [73]. That is to say, up to second-order approximation,

$$\delta g_{\mu\nu} \sim (\delta\psi)^2 + \cdots, \qquad (28)$$

where $\cdots$ represents all other possible perturbations. For any quantity $A(g_{\mu\nu})$ that only depend on the geometry, the perturbation will become,

$$\delta A = A' \delta g_{\mu\nu}. \qquad (29)$$

In the critical region, the condensate has $\sqrt{\langle O_2 \rangle}/\mu \sim t^{1/2}$, and hence $\psi \sim t^{1/2}$ [59]. Consequently, we will have $\delta A \sim t^1$. Therefore, the HEE, MI and EWCS all have the same scaling exponent 1. However, for systems with nonminimal coupling between matter term and the geometry, the HEE, MI and even EWCS will explicitly depend

on the matter field. In these theories, the critical behavior of entanglement-related quantities may be different.

From the perspective of quantum many body theory, similar critical phenomena can also be seen [2,74]. The explanation from quantum many body theory is that the correlation between entanglement-related physical quantities and the thermodynamic function of the system leads to these phenomena. From the perspective of holography, the entanglement-related physical quantities are mainly determined by the perturbation relation of the dependence of geometry and coherent field.

VII. DISCUSSION

We have investigated the HEE, MI and EWCS for general strip configurations in the superconductivity phase transition model. We find that HEE, MI and EWCS can all diagnose the superconducting phase transition. They are continuous at the critical point, but their first derivative with respect to temperature is discontinuous. Also, they all exhibit the same critical behavior due to the perturbation relationship between the geometry and the condensate. In addition, as a measure of entanglement of mixed states, MI exhibits the opposite behavior to HEE. Specifically, MI decreases with increasing temperature and exhibits a convex behavior, while HEE increases with increasing temperature and exhibits a concave behavior. These results do not depend on the specific configuration. Moreover, as a new measure of mixed state entanglement, EWCS can exhibit either the same or the opposite behavior as MI, depending on the size of the specific configuration. These results show that EWCS can not only describe the phase transition but also capture more abundant information than HEE and MI.

Thermal phase transition is usually accompanied by the emergence of order parameter [57], which is the main reason why HEE, MI and EWCS can diagnose it. However, not all phase transitions occur with the emergence of order parameters. Quantum phase transition occurs at zero temperature when changing system parameters. There are certain quantum phase transitions in which the order parameter is absent. Therefore, the characterization of these quantum phases becomes an important topic. Metal-insulator transition, as one of the most well-known quantum phase transition, was found intimately related to the EE [16–18]. However, EE cannot completely exclude the contribution of thermal entropy. As a new mixed state entanglement measure independent of the EE, we can expect that EWCS may play an important role in a quantum phase transition. This is the direction of our future efforts.

Another major advance of this paper is to provide an upgraded version of EWCS algorithms. Using these algorithms, the calculation of EWCS can be more stable and reliable, which can pave the way for further study of EWCS. For example, the properties of EWCS in Born-Infeld system, massive gravity and Lovelock gravity theory are all worth exploring. These studies will lay a foundation for a more comprehensive understanding of the properties of mixed state entanglement in more general holographic models.

[1] A. Osterloh, L. Amico, G. Falci, and R. Fazio, Scaling of entanglement close to a quantum phase transitions, Nature (London) **416**, 608 (2002).

[2] L. Amico, R. Fazio, A. Osterloh, and V. Vedral, Entanglement in many-body systems, Rev. Mod. Phys. **80**, 517 (2008).

[3] M. Levin and X.-G. Wen, Detecting Topological Order in a Ground State Wave Function, Phys. Rev. Lett. **96**, 110405 (2006).

[4] A. Kitaev and J. Preskill, Topological Entanglement Entropy, Phys. Rev. Lett. **96**, 110404 (2006).

[5] S. Ryu and T. Takayanagi, Holographic Derivation of Entanglement Entropy from AdS/CFT, Phys. Rev. Lett. **96**, 181602 (2006).

[6] V. E. Hubeny, M. Rangamani, and T. Takayanagi, A covariant holographic entanglement entropy proposal, J. High Energy Phys. 07 (2007) 062.

[7] A. Lewkowycz and J. Maldacena, Generalized gravitational entropy, J. High Energy Phys. 08 (2013) 090.

[8] X. Dong, A. Lewkowycz, and M. Rangamani, Deriving covariant holographic entanglement, J. High Energy Phys. 11 (2016) 028.

[9] G. Vidal and R. F. Werner, A computable measure of entanglement, Phys. Rev. A **65**, 032314 (2002).

[10] R. Horodecki, P. Horodecki, M. Horodecki, and K. Horodecki, Quantum entanglement, Rev. Mod. Phys. **81**, 865 (2009).

[11] T. Nishioka and T. Takayanagi, AdS bubbles, entropy and closed string tachyons, J. High Energy Phys. 01 (2007) 090.

[12] I. R. Klebanov, D. Kutasov, and A. Murugan, Entanglement as a probe of confinement, Nucl. Phys. **B796,** 274 (2008).

[13] A. Pakman and A. Parnachev, Topological entanglement entropy and holography, J. High Energy Phys. 07 (2008) 097.

[14] S. J. Zhang, Holographic entanglement entropy close to crossover/phase transition in strongly coupled systems, Nucl. Phys. **B916,** 304 (2017).

[15] X. X. Zeng and L. F. Li, Holographic phase transition probed by nonlocal observables, Adv. High Energy Phys. **2016,** 6153435 (2016).

[16] Y. Ling, P. Liu, C. Niu, J. P. Wu, and Z. Y. Xian, Holographic entanglement entropy close to quantum phase transitions, J. High Energy Phys. 04 (2016) 114.

[17] Y. Ling, P. Liu, and J. P. Wu, Characterization of quantum phase transition using holographic entanglement entropy, Phys. Rev. D **93,** 126004 (2016).

[18] Y. Ling, P. Liu, J. P. Wu, and Z. Zhou, Holographic metal-insulator transition in higher derivative gravity, Phys. Lett. B **766,** 41 (2017).

[19] X. M. Kuang, E. Papantonopoulos, and B. Wang, Entanglement entropy as a probe of the proximity effect in holographic superconductors, J. High Energy Phys. 05 (2014) 130.

[20] H. Guo, X. M. Kuang, and B. Wang, Holographic entanglement entropy and complexity in Stückelberg superconductor, Phys. Lett. B **797,** 134879 (2019).

[21] S. Mahapatra, Interplay between the holographic QCD phase diagram and mutual & n-partite information, J. High Energy Phys. 04 (2019) 137.

[22] X. Dong, The gravity dual of Renyi entropy, Nat. Commun. **7,** 12472 (2016).

[23] S. H. Shenker and D. Stanford, Black holes and the butterfly effect, J. High Energy Phys. 03 (2014) 067.

[24] Y. Sekino and L. Susskind, Fast Scramblers, J. High Energy Phys. 10 (2008) 065.

[25] J. Maldacena, S. H. Shenker, and D. Stanford, A bound on chaos, J. High Energy Phys. 08 (2016) 106.

[26] A. Donos and S. A. Hartnoll, Metal-insulator transition in holography, Nat. Phys. **9,** 649 (2013).

[27] M. Blake, Universal Charge Diffusion and the Butterfly Effect in Holographic Theories, Phys. Rev. Lett. **117,** 091601 (2016).

[28] M. Blake, Universal diffusion in incoherent black holes, Phys. Rev. D **94,** 086014 (2016).

[29] Y. Ling, P. Liu, and J. P. Wu, Holographic butterfly effect at quantum critical points, J. High Energy Phys. 10 (2017) 025.

[30] Y. Ling, P. Liu, and J. P. Wu, Note on the butterfly effect in holographic superconductor models, Phys. Lett. B **768,** 288 (2017).

[31] S. F. Wu, B. Wang, X. H. Ge, and Y. Tian, Collective diffusion and quantum chaos in holography, Phys. Rev. D **97,** 106018 (2018).

[32] P. Liu, C. Niu, and J. P. Wu, The effect of anisotropy on holographic entanglement entropy and mutual information, Phys. Lett. B **796,** 155 (2019).

[33] A. R. Brown, D. A. Roberts, L. Susskind, B. Swingle, and Y. Zhao, Complexity, action, and black holes, Phys. Rev. D **93,** 086006 (2016).

[34] A. R. Brown, D. A. Roberts, L. Susskind, B. Swingle, and Y. Zhao, Holographic Complexity Equals Bulk Action?, Phys. Rev. Lett. **116,** 191301 (2016).

[35] S. Chapman, H. Marrochio, and R. C. Myers, Complexity of formation in holography, J. High Energy Phys. 01 (2017) 062.

[36] Y. Ling, Y. Liu, and C. Y. Zhang, Holographic subregion complexity in Einstein-Born-Infeld theory, Eur. Phys. J. C **79,** 194 (2019).

[37] B. Chen, W. M. Li, R. Q. Yang, C. Y. Zhang, and S. J. Zhang, Holographic subregion complexity under a thermal quench, J. High Energy Phys. 07 (2018) 034.

[38] R. Q. Yang, H. S. Jeong, C. Niu, and K. Y. Kim, Complexity of holographic superconductors, J. High Energy Phys. 04 (2019) 146.

[39] Y. Ling, Y. Liu, C. Niu, Y. Xiao, and C. Y. Zhang, Holographic subregion complexity in general Vaidya geometry, J. High Energy Phys. 11 (2019) 039.

[40] Y. T. Zhou, X. M. Kuang, Y. Z. Li, and J. P. Wu, Holographic subregion complexity under a thermal quench in an Einstein-Maxwell-axion theory with momentum relaxation, Phys. Rev. D **101,** 106024 (2020).

[41] Y. T. Zhou, M. Ghodrati, X. M. Kuang, and J. P. Wu, Evolutions of entanglement and complexity after a thermal quench in massive gravity theory, Phys. Rev. D **100,** 066003 (2019).

[42] S. Chakrabortty, S. Pant, and K. Sil, Effect of back reaction on entanglement and subregion volume complexity in strongly coupled plasma, J. High Energy Phys. 06 (2020) 061.

[43] T. Takayanagi and K. Umemoto, Holographic entanglement of purification, Nat. Phys. **14,** 573 (2018).

[44] P. Nguyen, T. Devakul, M. G. Halbasch, M. P. Zaletel, and B. Swingle, Entanglement of purification: From spin chains to holography, J. High Energy Phys. 01 (2018) 098.

[45] J. Kudler-Flam and S. Ryu, Entanglement negativity and minimal entanglement wedge cross sections in holographic theories, Phys. Rev. D **99,** 106014 (2019).

[46] Y. Kusuki, J. Kudler-Flam, and S. Ryu, Derivation of Holographic Negativity in AdS$_3$/CFT$_2$, Phys. Rev. Lett. **123,** 131603 (2019).

[47] S. Dutta and T. Faulkner, A canonical purification for the entanglement Wedge cross-section, J. High Energy Phys. 03 (2021) 178.

[48] Y. F. Huang, Z. J. Shi, C. Niu, C. y. Zhang, and P. Liu, Mixed state entanglement for holographic axion model, Eur. Phys. J. C **80,** 426 (2020).

[49] G. Fu, P. Liu, H. Gong, X. M. Kuang, and J. P. Wu, Informational properties for Einstein-Maxwell-Dilaton gravity, arXiv:2007.06001.

[50] H. Gong, P. Liu, G. Fu, X. M. Kuang, and J. P. Wu, Informational properties of holographic Lifshitz field theory, Chin. Phys. C **45,** 065101 (2021).

[51] P. Liu, Y. Ling, C. Niu, and J. P. Wu, Entanglement of purification in holographic systems, J. High Energy Phys. 09 (2019) 071.

[52] A. Lala, Entanglement measures for non-conformal D-branes, Phys. Rev. D **102**, 126026 (2020).

[53] N. Bao and I. F. Halpern, Conditional and multipartite entanglements of purification and holography, Phys. Rev. D **99**, 046010 (2019).

[54] K. Umemoto and Y. Zhou, Entanglement of purification for multipartite states and its holographic dual, J. High Energy Phys. 10 (2018) 152.

[55] R. Q. Yang, C. Y. Zhang, and W. M. Li, Holographic entanglement of purification for thermofield double states and thermal quench, J. High Energy Phys. 01 (2019) 114.

[56] S. A. Hartnoll, C. P. Herzog, and G. T. Horowitz, Building a Holographic Superconductor, Phys. Rev. Lett. **101**, 031601 (2008).

[57] R. G. Cai, L. Li, L. F. Li, and R. Q. Yang, Introduction to holographic superconductor models, Sci. China Phys. Mech. Astron. **58**, 1 (2015).

[58] A. Donos and J. P. Gauntlett, Holographic Q-lattices, J. High Energy Phys. 04 (2014) 040.

[59] H. B. Zeng, X. Gao, Y. Jiang, and H. S. Zong, Analytical computation of critical exponents in several holographic superconductors, J. High Energy Phys. 05 (2011) 002.

[60] M. A. Nielsen and C. Isaac, Quantum computation and quantum information, Am. J. Phys. 558 (2002).

[61] B. M. Terhal, M. Horodecki, D. W. Leung, and D. P. DiVincenzo, The entanglement of purification, J. Math. Phys. (N.Y.) **43**, 4286 (2002).

[62] N. Bao and I. F. Halpern, Holographic inequalities and entanglement of purification, J. High Energy Phys. 03 (2018) 006.

[63] Y. Ling, Y. Liu, and Z. Y. Xian, Entanglement entropy of annulus in holographic thermalization, Chin. Phys. C **44**, 023101 (2020).

[64] J. P. Boyd, *Chebyshev and Fourier Spectral Methods* (Dover Publications, New York, 2001).

[65] A. Almheiri, R. Mahajan, J. Maldacena, and Y. Zhao, The Page curve of Hawking radiation from semiclassical geometry, J. High Energy Phys. 03 (2020) 149.

[66] A. Almheiri, R. Mahajan, and J. Maldacena, Islands outside the horizon, arXiv:1910.11077.

[67] H. Z. Chen, R. C. Myers, D. Neuenfeld, I. A. Reyes, and J. Sandor, Quantum extremal islands made easy. Part I. Entanglement on the brane, J. High Energy Phys. 10 (2020) 166.

[68] J. Kudler-Flam, Y. Kusuki, and S. Ryu, Correlation measures and the entanglement wedge cross-section after quantum quenches in two-dimensional conformal field theories, J. High Energy Phys. 04 (2020) 074.

[69] R. G. Cai, S. He, L. Li, and Y. L. Zhang, Holographic entanglement entropy in insulator/superconductor transition, J. High Energy Phys. 07 (2012) 088.

[70] R. G. Cai, S. He, L. Li, and Y. L. Zhang, Holographic entanglement entropy on P-wave superconductor phase transition, J. High Energy Phys. 07 (2012) 027.

[71] Y. Peng, Holographic entanglement entropy in superconductor phase transition with dark matter sector, Phys. Lett. B **750**, 420 (2015).

[72] W. Yao and J. Jing, Holographic entanglement entropy in metal/superconductor phase transition with exponential nonlinear electrodynamics, Phys. Lett. B **759**, 533 (2016).

[73] R. Brito, V. Cardoso, and P. Pani, Superradiance: New frontiers in black hole physics, Lect. Notes Phys. **906**, 1 (2015).

[74] K.-H. Wu, T.-C. Lu, C.-M. Chung, Y.-J. Kao, and T. Grover, Entanglement Renyi Negativity Across a Finite Temperature Transition: A Monte Carlo Study, Phys. Rev. Lett. **125**, 140603 (2020).